ACS APPLIED MATERIALS & INTERFACES

Research Article

www.acsami.org

Alternative Synthesis of $CuFeSe_2$ Nanocrystals with Magnetic and Photoelectric Properties

Wenliang Wang,[†,‡,§,∥] Jun Jiang,[†,‡,§,∥] Tao Ding,[†,‡,§,∥] Chunde Wang,[†,‡,§,∥] Jian Zuo,[†] and Qing Yang*[,†,‡,§,∥]

[†]Hefei National Laboratory of Physical Sciences at the Microscale, [‡]Department of Chemistry, [§]Laboratory of Nanomaterials for Energy Conversion, and [∥]Synergetic Innovation Center of Quantum Information & Quantum Physics, University of Science and Technology of China (USTC), Hefei 230026, Anhui, P. R. China

Supporting Information

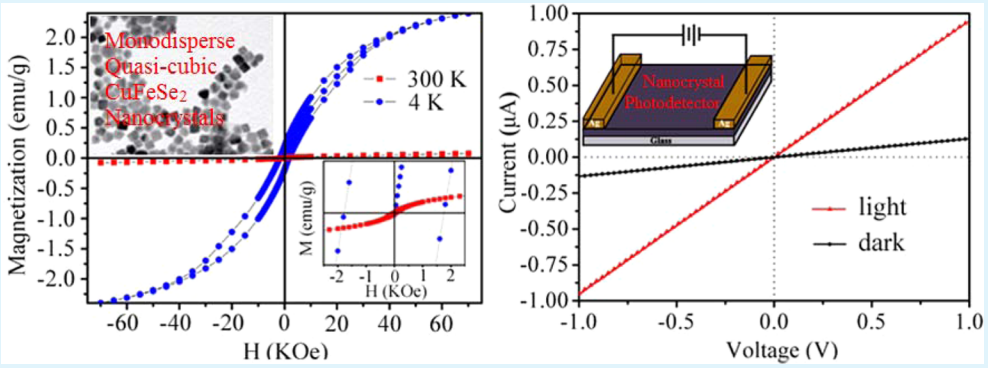

ABSTRACT: Monodisperse $CuFeSe_2$ nanocrystals of high quality have been successfully synthesized for the first time using a hot-solution injection method from the reaction of metallic acetylacetonates with diphenyl diselenide (Ph_2Se_2) in oleylamine with addition of oleic acid at 255 °C for 90 min. The characterizations of X-ray diffraction, electron microscopy, and compositional analysis reveal that the resulting $CuFeSe_2$ nanocrystals are of tetragonal phase with a stoichiometric composition. The $CuFeSe_2$ nanocrystals exhibit well-defined quasi-cubic shape with an average size of ~18 nm, and their shape can be tuned from quasi-cubes to quasi-spheres by adjusting the reaction parameters. Magnetic measurement reveals that the as-synthesized $CuFeSe_2$ nanocrystals are ferromagnetic and paramagnetic at 4 and 300 K, respectively. Additionally, the current−voltage (I−V) behavior of the $CuFeSe_2$ nanocrystals suggests that they are promising candidates for application in optoelectronics and solar energy conversion.

KEYWORDS: *monodisperse $CuFeSe_2$ nanocrystal, eskebornite, ternary selenide, magnetic property, narrow bandgap semiconductor, optoelectronic property, photodetector, organometallic synthesis*

1. INTRODUCTION

As a result of unique chemical and physical properties including high absorption coefficients, high conversion efficiency, and low toxicity,[1−5] there has been widespread interest in the synthesis of I−III−VI_2 group ternary chalcogenides. For example, $CuFeS_2$ nanoparticles,[6−9] nanorods,[10,11] and nanowires[12] have been achieved via the solution-based synthetic route. Meanwhile, $CuInS_2$, $CuInSe_2$, and $AgInS_2$ have also been fabricated from different specific solution strategies.[11−13] It is interesting that these ternary chalcogenides demonstrate wide potential in the fields of fabrication of solar cells, photodetectors, and nonlinear optical devices.[13−17] Very recently, these ternary chalcopyrites of $CuInS_2$, $CuInSe_2$, $AgInS_2$, and $CuFeS_2$ nanostructures have been explored for the fabrication of photovoltaic solar cells,[18−21] bioimaging probes,[22] and thermoelectric devices.[6] However, among the I−III−VI_2 group ternary chalcogenides, less attention been paid to $CuFeSe_2$, as known eskebornite with a narrow band gap of 0.16 eV for the bulk,[23] even though the eskebornite $CuFeSe_2$ is thought to be one of the most promising materials due to its possible optical, electric, and magnetic properties. In general, it is difficult to synthesize phase-pure and monodisperse $CuFeSe_2$ nanocrystals (NCs) in an actual process due to the difficulty in choosing the relatively high reactivity-matching of reaction precursors, although solvothermal[24,25] and solid-state reaction[26,27] have been proposed for the production of $CuFeSe_2$ NCs for a long time. It is noted that the $CuFeSe_2$ NCs obtained from these routes[24−27] are commonly out of shape with irregular, large size and size distribution, and even attached to each other to form very large aggregates, which would restrict their potential applications in the confined dimensions. As we known, the size, shape, composition, monodispersity, and surface structures in

Received: August 21, 2014
Accepted: January 6, 2015
Published: January 6, 2015

DOI: 10.1021/am508844w
ACS Appl. Mater. Interfaces 2015, 7, 2235−2241

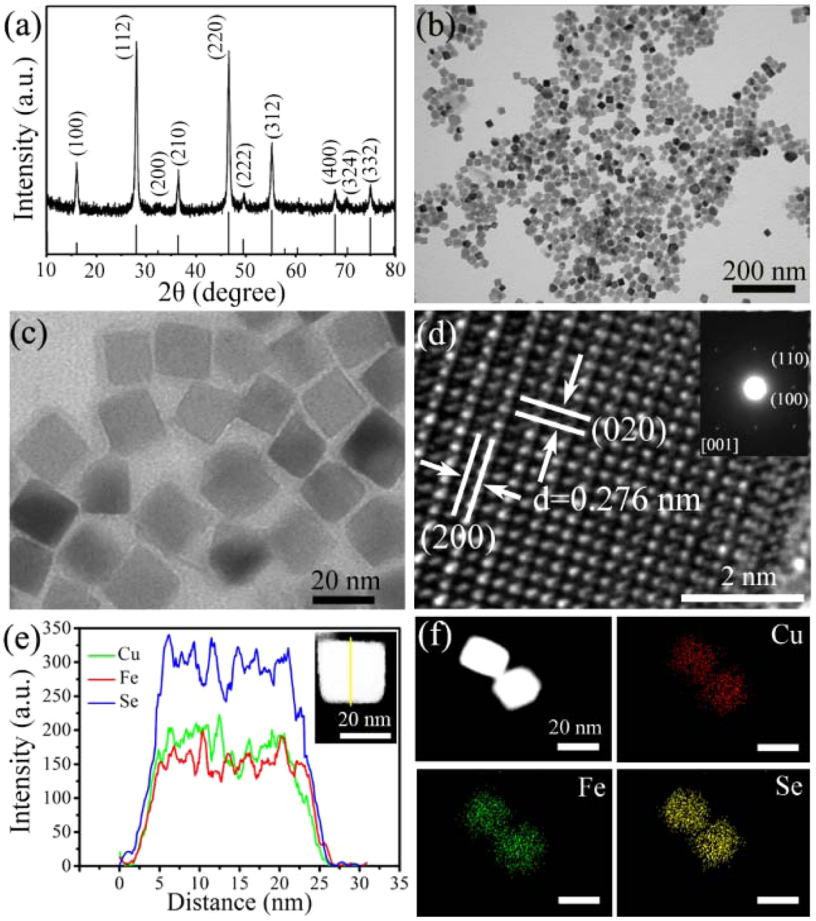

Figure 1. (a) XRD pattern, (b) low-magnification TEM, (c) high-magnification TEM image of the $CuFeSe_2$ NCs, (d) HRTEM image of an individual nanostructured crystal with inserted corresponding SAED pattern, (e) STEM-EDX line scan of the individual $CuFeSe_2$ nanocrystal, and (f) HAADF-STEM and EELS elemental mapping images of the ternary $CuFeSe_2$ NCs.

addition to synthetic strategy of the semiconductor NCs would intensively influence their variety of physical and chemical properties and even affect their functionalities and potential applications. Therefore, the synthesis exploring for such ternary nanomaterials is highly desirable, and also their controllable synthesis with high monodispersity, uniform size, and specific shapes will be of more importance for the application of such ternary nanostructures.

It is well-known that the hot-solution-injection-based method usually provides a more controllable tool for the growth of nanostructures with confined size and shape in addition to high monodispersity, and it has been widely used for the production of monodisperse $CuInSe_2$ and $Cu_{2-x}Se$ NCs.[15,19,28−30] Inspired by the advantages of such a hot-solution-injection strategy, in this study, we have prepared $CuFeSe_2$ NCs via an alternative hot-solution-injection-based synthetic process, in which the $CuFeSe_2$ NCs are obtained from the reaction of metallic acetylacetonates with diphenyl diselenide (Ph_2Se_2) in oleylamine with addition of oleic acid at 255 °C for 90 min. As expected, this is a facile, safe, and cost-effective synthetic route for the controllable growth of $CuFeSe_2$ NCs, and the as-synthesized $CuFeSe_2$ NCs are of high monodispersity with uniform size and tunable shape. Moreover, the optoelectronic properties of $CuFeSe_2$ NCs have been first investigated and it is found that the $CuFeSe_2$ NCs can be applied technically as photovoltaic devices.

2. EXPERIMENTAL SECTION

2.1. Chemicals. Copper(II) acetylacetone ($Cu(II)(acac)_2$, 98%), diphenyl diselenide (Ph_2Se_2, 98%), and iron(III) acetylacetonate ($Fe(III)(acac)_3$) were ordered from Alfa Aesar. Oleylamine (OAm, 70%) and oleic acid (OA, 90%) were purchased from Aldrich. Absolute ethanol, tetrachloroethylene, and toluene were obtained from Sinopharm Chemical Reagent Ltd., China. All chemicals were used in the experiments without further purification.

2.2. Synthesis of Typical Quasi-Cubic-Shaped $CuFeSe_2$ Nanocrystals. In a typical synthesis, $Cu(II)(acac)_2$ (0.046 g, 0.175 mmol), Ph_2Se_2 (0.078 g, 0.250 mmol), 0.5 mL of OA, and 7.5 mL of OAm were added into a three-neck 50 mL round-bottom flask at room temperature. The mixture was first heated to 140 °C for 30 min under an argon flow and magnetic stirring to remove water and other low-boiling-point impurities. The Fe precursor solution was freshly prepared and preheated to 70 °C by mixing 0.088 g of $Fe(III)(acac)_3$ (0.250 mmol) with 2.0 mL of OAm. Then, the Fe-precursor solution was transferred into a syringe equipped with a large needle and injected quickly into the flask at 210 °C. The mixture was further heated to 255 °C and kept at that temperature for 90 min, and then cooled to room temperature naturally. The product was collected by centrifugation (9000 rpm, 4 min) and washed several times with absolute ethanol and toluene. The final samples were dispersed in toluene or tetrachloroethylene for further characterization.

2.3. Characterization. The samples were characterized by X-ray power diffraction (XRD), using a Philips X'Pert PRO SUPER X-ray diffractometer equipped with graphite monochromaticized Cu Kα radiation (λ = 1.54056 Å). The operation voltage and current were kept at 40 kV and 400 mA, respectively. Transmission electron microscopy (TEM), high-resolution transmission electron microscopy

DOI: 10.1021/am508844w
ACS Appl. Mater. Interfaces 2015, 7, 2235−2241

(HRTEM), and the corresponding selected-area electron diffraction (SAED) were performed on Hitachi H-7650 and JEOL 2010 with an acceleration voltage of 200 kV, respectively. The compositions of the samples were investigated by energy dispersive X-ray spectroscopy (EDX, OXFORD INCA system), high-angle annular dark-field imaging in the scanning TEM (HAADF-STEM), and electron energy loss spectroscopy (EELS). X-ray photoelectron spectroscopy (XPS) was acquired on an ESCALAB MK II with Mg Kα as the excitation source. Inductively coupled plasma atomic emission spectroscopy (ICP-AES) analysis performed on PerkinElmer Model Optima 3000DV was used to quantify the composition of the NCs. The surface structures of the samples were determined by attenuated total reflection Fourier transformed infrared (ATR-FTIR) spectroscopy (Prestige-21, SHIMADZU). Thermogravimetric analysis (TGA) was carried out on a TGA-60 thermal analyzer (Shimadzu Corporation) with a heating rate of 10 °C/min in flowing nitrogen. The magnetic measurements on powder samples enclosed in a medical cap were carried out with a vibrating sample magnetometer (VSM). Optical absorption spectra were recorded on a spectrophotometer (DUV−3700 UV−vis-NIR) from 400 to 2400 nm at room temperature. Current−voltage (I−V) characteristics of the devices were recorded with a two-probe method using an electrochemical station (CHI660e) and xenon lamp (PLS-SXE300) was selected as a white light source in a shielded and clean box at room temperature.

3. RESULTS AND DISCUSSION

3.1. XRD and TEM Analysis. The phase of the as-synthesized NCs was characterized by XRD. As shown in Figure 1a, all the diffraction peaks are in good agreement with the standard data of tetragonal phase $CuFeSe_2$ in eskebornite form (JCPDS No. 81−1959), indicating that the as-synthesized $CuFeSe_2$ NCs are of high purity and good crystallinity. The morphology of the as-prepared $CuFeSe_2$ NCs was examined by TEM. As displayed in Figure 1b and c, the as-synthesized NCs present a monodisperse and uniform quasi-cubic shape with an average diameter of about 18 nm based on statistic histogram of size distribution, as shown in Figure S1 in the Supporting Information. Figure 1d displays an HRTEM image of an individual nanocrystal. The clear lattice fringes show that the NCs are well crystallized, and the observed d-spacings (about 0.276 nm) correspond to the (200) and (020) planes of the tetragonal-phase $CuFeSe_2$. The corresponding SAED pattern in the [001] zone axis as shown in the inset of Figure 1d further indicates that the tetragonal $CuFeSe_2$ nanostructures are of single-crystalline nature. At the same time, energy dispersive X-ray spectroscopic (EDX), STEM-EDX line, and EELS elemental mapping measurements were performed to identify the composition and verify the presence of the three elements in each individual nanocrystal for the $CuFeSe_2$ NCs. In Supporting Information Figure S2, the EDX spectrum shows that three elements of Cu, Fe, and Se are coexistent in the as-synthesized $CuFeSe_2$ NCs, and the molar ratio is determined as 1.02:1:2.04 for Cu:Fe:Se, consistent with the stoichiometric composition of $CuFeSe_2$. Figure 1e and f presents the STEM-EDX line of a typical $CuFeSe_2$ NC and the EELS elemental mapping of the $CuFeSe_2$ NCs, respectively, and they both reveal that the $CuFeSe_2$ NCs have homogeneous distribution of three elements of Cu, Fe, and Se with molar ratio close to the expected 1:1:2.

3.2. Mössbauer and ICP-AES Determination. To reveal the oxidation state of Fe element in the as-obtained $CuFeSe_2$ NCs, Mössbauer spectroscopic measurements were performed at room temperature. As displayed in Figure 2, iron occupies two different sites, indicating the oxidation state of +3 for Fe. This measurement is also consistent with the results in the reported literature.[24,31,32] In addition, from the XPS characterization (Supporting Information Figure S3) and detailed discussion in Supporting Information, it can be deduced that the valence states of Cu, Fe, and Se are +1, +3, and −2, respectively. Meanwhile, the chemical composition of the $CuFeSe_2$ NCs was also determined by inductively coupled plasma atomic emission (ICP-AES). As shown in Supporting Information Table S1, the elemental compositions of the as-prepared $CuFeSe_2$ NCs are 1:1.01:1.90 for molar ratio of Cu:Fe:Se, which is close to the results from EDX measurements (Figure 1e,f and Supporting Information Figure S2).

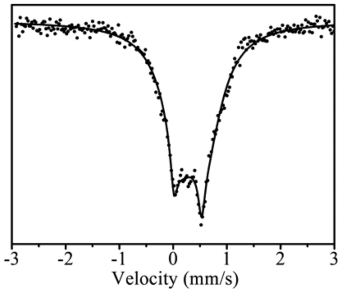

Figure 2. Mössbauer spectrum of the as-obtained $CuFeSe_2$ NCs measured at room temperature.

3.3. Formation and Morphological Evolution. It is noted that the main problem for the synthesis of ternary chalcogenides lies in controlling and limiting the phase separation of the ternaries via solution-phase strategies at relative low temperatures.[33−36] In the present route, the monodisperse $CuFeSe_2$ NCs are successfully achieved from the reaction of metallic acetylacetonates of Cu(II) and Fe(III) with Ph_2Se_2 in oleylamine with the addition of oleic acid at 255 °C for 90 min as optimal reaction conditions on the basis of intensive investigations as demonstrated in Supporting Information Figure S4. It is worth noting that the reaction time plays a significant role in regulating the size, shape, and purity of the as-synthesized ternary $CuFeSe_2$ NCs (Supporting Information Figure S4). Meanwhile, the final formation of the ternary $CuFeSe_2$ NCs without phase separation is due to the almost equivalent reactivity of the selenium source of Ph_2Se_2 with the two employed metallic sources in the synthetic system. Importantly, such conditions with reactivity-matching metallic sources are favorable for the growth of the ternary $CuFeSe_2$ NCs with homogeneous nanostructures, which are supported by EDX measurements as seen in Figure 1. This phenomenon has also been reported in various ternary systems in the literature.[15,37]

In addition, the purity of the phase as well as the shape of the as-synthesized nanoparticles can be tunable by changing the ratio of precursors and capping ligands. Experimental investigations determine that the pure $CuFeSe_2$ NCs with homogeneous structure are optimally synthesized in the process with a feedstock molar ratio of 0.7:1.0:2.0 for Cu, Fe, and Se from the precursors. When the precursor molar ratio of Cu:Fe:Se is set to 1:1:2 (stoichiometric ratio in $CuFeSe_2$), the obtained products are $CuFeSe_2$ NCs mixed with byproducts of Cu_2Se NCs as impurities, as displayed in Figure S5 in the Supporting Information. The reason for the products with impurity and/or phase separation from the stoichiometric feedstock is mainly the slightly weaker reactivity of iron(III) precursor than that of the Cu(II) source in addition to the step release of Se atoms from the selenium source of Ph_2Se_2.[37] To

DOI: 10.1021/am508844w
ACS Appl. Mater. Interfaces 2015, 7, 2235−2241

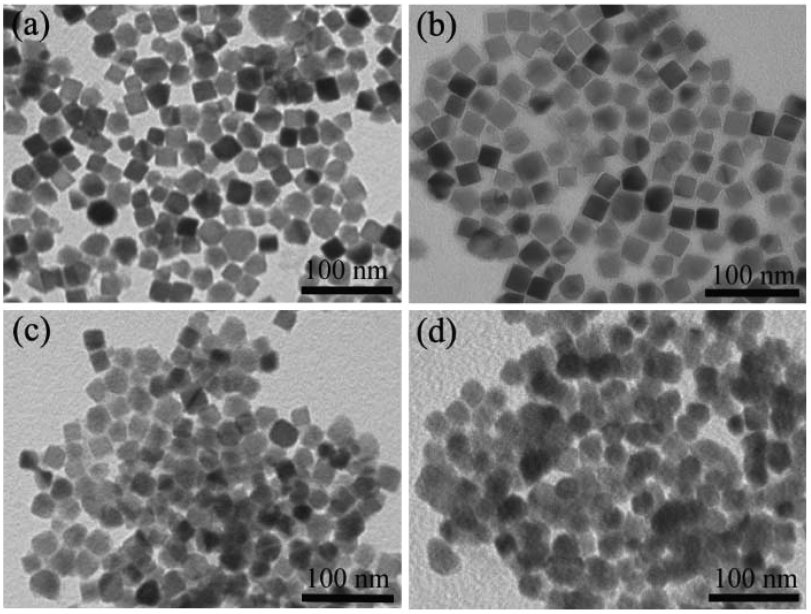

Figure 3. TEM images of $CuFeSe_2$ NCs shape evolution with the increasing of the concentration of OA: (a) in pure OAm (8.0 mL), (b) in OAm (7.5 mL) with OA (0.5 mL), (c) in OAm (7.0 mL) with OA (1.0 mL), and (d) in OAm (6.0 mL) with OA (2.0 mL).

achieve $CuFeSe_2$ NCs with high quality and high purity, we control the synthesis in the route by reducing the feedstock of the Cu(II) source, accordingly. Meanwhile, the influence of OA on $CuFeSe_2$ morphology evolution is also studied via using varied amounts of OA in the reaction process. As displayed in Figure 3a–d, the morphologies of the $CuFeSe_2$ NCs are varied from the media of pure OAm (8.0 mL without use of OA) to that of OAm (6.0 mL) in addition of OA (2.0 mL) on the basis of TEM observation. In detail, the prepared $CuFeSe_2$ NCs are quasi-cubes with a large proportion of irregular, large nanoparticles, but their structure is still in tetragonal eskebornite phase (Figure 3a). It is interesting that the $CuFeSe_2$ NCs demonstrated better monodispersity and morphological homogeneity when a trace of OA was added into the reaction system (Figure 3b), as compared to those without OA (Figure 3a). The capping effect of OA with appropriate concentration is favorable for the synthesis of $CuFeSe_2$ NCs with high monodispersity,[38] which is also supported by the ATR-FTIR determination (Supporting Information Figure S6). However, with the increase of the OA concentration, the resulting NCs become polydisperse and polyaggregated, and their shapes changed from quasi-cubes to nearly quasi-spheres (Figure 3c,d) due to the intensive interaction between metal ions and OA in the reaction system. Such a phenomenon has also been observed in early investigation.[39]

3.4. Magnetic and Optoelectronic Property. The magnetic properties of the $CuFeSe_2$ NCs are investigated via employing the vibrating sample magnetometer. Figure 4 shows the field loops of the synthesized $CuFeSe_2$ NCs at 4 and 300 K, respectively. At both temperatures, the field loop has a slanted appearance at high field, indicating the presence of a paramagnetic component, which is not saturated at 70 000 Oe. The zoom region between −2500 and 2500 Oe was shown in the inset of Figure 4 in order to show more clearly the hysteresis loops for 4 and 300 K, respectively. The coercivity sharply increases from 39 Oe at 300 K to 1780 Oe at 4 K, probably due to the reduced thermal fluctuation of magnetic

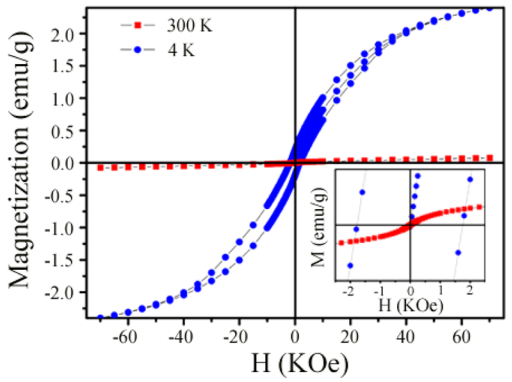

Figure 4. Magnetic behavior of the $CuFeSe_2$ NCs. M–H curves of $CuFeSe_2$ recorded at 4 and 300 K, respectively.

dipoles.[35] In addition, with regard to magnetic properties of $CuFeSe_2$, previous reports showed paramagnetic behavior from room temperature down to a temperature of ∼71 K, where a magnetic transition occurred. Below this temperature, the behavior appeared to indicate a weak ferrimagnetic or very weak ferromagnetic form.[32] Moreover, Woolley et al. reported that a magnetic transition occurs in $CuFeSe_2$ at approximately 80 K. The Fe atoms on the 2e and 2a sites (of the tetragonal cell) have slightly different magnetic moments, resulting in a weak ferrimagnetic behavior.[40] The average magnetic moment of Fe atoms was ∼1.75 μ_B, with a direction at an angle of ∼15° to the $y-z$ plane. In the current work, the magnetic moment of Fe^{3+} in the $CuFeSe_2$ nanocrystals is calculated to be 0.12 μ_B (4 K), probably indicating a very weak ferromagnetic property. The reduced moment compared to previous reports may be attributed to the size and surface effects of the $CuFeSe_2$ nanostructures with small size and dimension. As we noted, when materials that exhibit magnetic properties are reduced within nanometer scale size, the nanostructured materials will strongly differ from their corresponding bulk materials due to size effects, surface effects, and interparticle interactions.[41−43]

DOI: 10.1021/am508844w
ACS Appl. Mater. Interfaces 2015, 7, 2235−2241

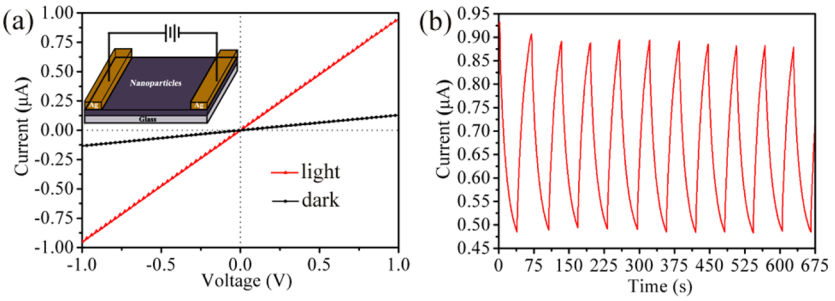

Figure 5. (a) $I-V$ curves of the $CuFeSe_2$ NCs thin film device in the dark state and under xenon lamp illumination, and (b) time-dependent response of the photoresponse device measured under air conditions at a bias of 1.0 V; the light power intensity was kept at 12 mW cm^{-2} when the xenon lamp was turned on. The inset in (a) shows schematics of device configuration for photoresponse measurement.

More complete reviews can be found elsewhere on magnetism in nanoscale systems.[44]

The optical property investigation of the as-synthesized $CuFeSe_2$ NCs (Supporting Information Figure S7) indicates that they have potential application in optoelectronic conversion in addition to solar energy conversion. To evaluate the optoelectronic application of the as-prepared $CuFeSe_2$ NCs, a photoresponse device was fabricated as shown in Figure 5a, where the film was prepared by drop-casting concentrated toluene solution of $CuFeSe_2$ nanoparticles on glass. Then, the silver electrodes were fabricated using silver paste attached conducting silver wires on the film. A xenon lamp was used as a white-light source. Figure 5a shows the $I-V$ curves of the devices exposed to white light and under dark conditions at a bias of 1.0 V. It was found that the current of $CuFeSe_2$ film increased from 0.13 μA in the dark to 0.94 μA when the xenon lamp was on, corresponding to a 7.2-fold increase. The increment of photocurrent under the xenon lamp was mainly attributed to an optical effect rather than a thermal effect (Supporting Information Figure S8). The time-dependent photoresponse of the device is shown in Figure 5b. This was measured by periodically turning the xenon lamp on and off under air conditions. Upon illumination, the photocurrent increased to a stable value of 0.90 μA. In a short test time cycle, although the current when the light was turned off has not dramatically decreased its initial dark station minimum value, the device still showed excellent stability and reproducibility.

To further improve the conductivity of the $CuFeSe_2$ NCs, a method of thermal annealing to remove capping agents was employed. Namely, the obtained $CuFeSe_2$ NCs were heated to 380 °C for 2 h under an argon flow inside a tube furnace. According to thermal analysis of TGA (Supporting Information Figure S9a), in contrast to unannealed sample the mass loss of the annealed $CuFeSe_2$ NCs did not show an obvious change when the temperature was heated at 380 °C, indicating that the large extent of surface organic capping agents were removed. In addition, the annealing process did not appreciably alter the phase of the $CuFeSe_2$ NCs as observed from the XRD patterns (Supporting Information Figure S9b). On the basis of the results stated above, the as-obtained $CuFeSe_2$ NCs could stabilize at the high temperature since their size and size distribution remains almost constant after thermal treatment at 380 °C for 2 h (Supporting Information Figure S10). The annealed $CuFeSe_2$ nanoparticles were fabricated to film in the same way as described above. With the optimized post-treatment, the photocurrent of the thermal annealing-processed $CuFeSe_2$ film could approach 13.3 μA at a bias of 1.0 V as shown in Figure S11 in the Supporting Information. The optimized $CuFeSe_2$ photoresponse device showed a promising increase in current by ca. 14 times under light illumination as compared to the one without annealing treatment (Figure 5).

4. CONCLUSIONS

In this study, we have first developed an alternative simple and convenient solution method to synthesize the high-quality $CuFeSe_2$ NCs with monodisperse size and uniform quasi-cubic shape. The crystal phase and shapes of the nanocrystals can be controlled by adjusting the proportion of precursors and capping agents in feedstocks. Meanwhile, magnetic measurements show that the as-prepared $CuFeSe_2$ NCs are ferromagnetic at low temperature but paramagnetic at room temperature. Additionally, optoelectronic measurements make them promising as potential candidates for the development of photovoltaic devices since their photoresponse can be highly improved under light illumination.

■ ASSOCIATED CONTENT

Supporting Information

Statistic histogram of size distribution; EDX patterns, XPS, ICP-AES, UV−vis-NIR, and ATR-FTIR spectra of the as-synthesized $CuFeSe_2$ NCs; XRD patterns and TEM images of the $CuFeSe_2$ NCs synthesized at 255 °C with different reaction times; influence of the thermal effect from xenon lamp illumination on the electroconductibility of the semiconducting $CuFeSe_2$ nanocrystals; XRD patterns of the $CuFeSe_2$ NCs synthesized under the condition with molar ratio of 1:1:2 for Cu:Fe:Se in feedstock in addition to TEM image of the annealed sample at 380 °C; TGA and $I-V$ curves of the $CuFeSe_2$ NCs before and after 380 °C annealing. This material is available free of charge via the Internet at http://pubs.acs.org.

■ AUTHOR INFORMATION

Corresponding Author

*E-mail: qyoung@ustc.edu.cn. Tel.: +86-551-63600243. Fax: +86-551-63606266.

Notes

The authors declare no competing financial interest.

■ ACKNOWLEDGMENTS

This work was supported by the National Basic Research Program of China (2012CB922001) and the National Nature Science Foundation of China (51271173, 21071136). We thank Prof. Shuji Ye in USTC for technical assistance on ATR-FTIR measurements.

DOI: 10.1021/am508844w
ACS Appl. Mater. Interfaces 2015, 7, 2235−2241

REFERENCES

(1) Rockett, A.; Birkmire, R. W. $CuInSe_2$ for Photovoltaic Applications. *J. Appl. Phys.* **1991**, *70*, R81−R97.

(2) Yu, L.; Kokenyesi, R. S.; Keszler, D. A.; Zunger, A. Inverse Design of High Absorption Thin-Film Photovoltaic Materials. *Adv. Energy Mater.* **2013**, *3*, 43−48.

(3) Jackson, P.; Hariskos, D.; Lotter, E.; Paetel, S.; Wuerz, R.; Menner, R.; Wischmann, W.; Powalla, M. New World Record Efficiency for $Cu(In,Ga)Se_2$ Thin-Film Solar Cells beyond 20%. *Progress in Photovoltaics: Research and Applications* **2011**, *19*, 894−897.

(4) Repins, I.; Contreras, M. A.; Egaas, B.; DeHart, C.; Scharf, J.; Perkins, C. L.; To, B.; Noufi, R. 19.9%-Efficient $ZnO/CdS/CuInGaSe_2$ Solar Cell with 81.2% Fill Factor. *Progress in Photovoltaics: Research and Applications* **2008**, *16*, 235−239.

(5) Lim, Y. S.; Kwon, H.-S.; Jeong, J.; Kim, J. Y.; Kim, H.; Ko, M. J.; Jeong, U.; Lee, D.-K. Colloidal Solution-Processed $CuInSe_2$ Solar Cells with Significantly Improved Efficiency up to 9% by Morphological Improvement. *ACS Appl. Mater. Interfaces* **2014**, *6*, 259−267.

(6) Liang, D.; Ma, R.; Jiao, S.; Pang, G.; Feng, S. A Facile Synthetic Approach for Copper Iron Sulfide Nanocrystals with Enhanced Thermoelectric Performance. *Nanoscale* **2012**, *4*, 6265−6268.

(7) Chen, K.-t.; Chiang, C.-J.; Ray, D. Hydrothermal Synthesis of Chalcopyrite Using an Environmental Friendly Chelating Agent. *Mater. Lett.* **2013**, *95*, 172−174.

(8) Silvester, E. J.; Healy, T. W.; Grieser, F.; Sexton, B. A. Hydrothermal Preparation and Characterization of Optically Transparent Colloidal Chalcopyrite ($CuFeS_2$). *Langmuir* **1991**, *7*, 19−22.

(9) Wang, Y.-H. A.; Bao, N.; Gupta, A. Shape-Controlled Synthesis of Semiconducting $CuFeS_2$ Nanocrystals. *Solid State Sci.* **2010**, *12*, 387−390.

(10) Disale, S. D.; Garje, S. S. A Convenient Synthesis of Nanocrystalline Chalcopyrite, $CuFeS_2$ Using Single-Source Precursors. *Appl. Organomet. Chem.* **2009**, *23*, 492−497.

(11) Hu, J.; Lu, Q.; Deng, B.; Tang, K.; Qian, Y.; Li, Y.; Zhou, G.; Liu, X. A Hydrothermal Reaction to Synthesize $CuFeS_2$ Nanorods. *Inorg. Chem. Commun.* **1999**, *2*, 569−571.

(12) Wang, M.; Wang, L.; Yue, G.; Wang, X.; Yan, P.; Peng, D. Single Crystal of $CuFeS_2$ Nanowires Synthesized through Solventothermal Process. *Mater. Chem. Phys.* **2009**, *115*, 147−150.

(13) Xu, J.; Luan, C.-Y.; Tang, Y.-B.; Chen, X.; Zapien, J. A.; Zhang, W.-J.; Kwong, H.-L.; Meng, X.-M.; Lee, S.-T.; Lee, C.-S. Low-Temperature Synthesis of $CuInSe_2$ Nanotube Array on Conducting Glass Substrates for Solar Cell Application. *ACS Nano* **2010**, *4*, 6064−6070.

(14) Li, L.; Coates, N.; Moses, D. Solution-Processed Inorganic Solar Cell Based on in Situ Synthesis and Film Deposition of $CuInS_2$ Nanocrystals. *J. Am. Chem. Soc.* **2010**, *132*, 22−23.

(15) Wang, J.-J.; Wang, Y.-Q.; Cao, F.-F.; Guo, Y.-G.; Wan, L.-J. Synthesis of Monodispersed Wurtzite Structure $CuInSe_2$ Nanocrystals and Their Application in High-Performance Organic-Inorganic Hybrid Photodetectors. *J. Am. Chem. Soc.* **2010**, *132*, 12218−12221.

(16) Omata, T.; Nose, K.; Otsuka-Yao-Matsuo, S. Size Dependent Optical Band Gap of Ternary I-III-VI_2 Semiconductor Nanocrystals. *J. Appl. Phys.* **2009**, *105*, 073106.

(17) Takeya, K.; Takemoto, Y.; Kawayama, I.; Murakami, H.; Matsukawa, T.; Yoshimura, M.; Mori, Y.; Tonouchi, M. Terahertz Emission from Coherent Phonons in Lithium Ternary Chalcopyrite Crystals Illuminated by 1560 nm Femtosecond Laser Pulses. *Europhys. Lett.* **2010**, *91*, 20004.

(18) Tapley, A.; Vaccarello, D.; Hedges, J.; Jia, F.; Love, D. A.; Ding, Z. Preparation and Characterization of $CuInS_2$ Nanocrystals for Photovoltaic Materials. *Phys. Chem. Chem. Phys.* **2013**, *15*, 1431−1436.

(19) Reifsnyder, D. C.; Ye, X.; Gordon, T. R.; Song, C.; Murray, C. B. Three-Dimensional Self-Assembly of Chalcopyrite Copper Indium Diselenide Nanocrystals into Oriented Films. *ACS Nano* **2013**, *7*, 4307−4315.

(20) Xu, L.-C.; Wang, R.-Z.; Liu, L.-M.; Chen, Y.-P.; Wei, X.-L.; Yan, H.; Lau, W.-M. Wurtzite-Type $CuInSe_2$ for High-Performance Solar Cell Absorber: ab initio Exploration of the New Phase Structure. *J. Mater. Chem.* **2012**, *22*, 21662−21666.

(21) Kim, S.; Kang, M.; Kim, S.; Heo, J.-H.; Noh, J. H.; Im, S. H.; Seok, S. I.; Kim, S.-W. Fabrication of $CuInTe_2$ and $CuInTe_{2-x}Se_x$ Ternary Gradient Quantum Dots and Their Application to Solar Cells. *ACS Nano* **2013**, *7*, 4756−4763.

(22) Chang, J.-Y.; Wang, G.-Q.; Cheng, C.-Y.; Lin, W.-X.; Hsu, J.-C. Strategies for Photoluminescence Enhancement of $AgInS_2$ Quantum Dots and their Application as Bioimaging Probes. *J. Mater. Chem.* **2012**, *22*, 10609−10618.

(23) Hamdadou, N.; Morsli, M.; Khelil, A.; Bernède, J. C. Fabrication of n-and p-Type Doped $CuFeSe_2$ Thin Films Achieved by Selenization of Metal Precursors. *J. Phys. D: Appl. Phys.* **2006**, *39*, 1042−1049.

(24) Lu, Q.; Hu, J.; Tang, K.; Deng, B.; Qian, Y.; Li, Y. The Synthesis of $CuFeSe_2$ through a Solventothermal Process. *J. Cryst. Growth* **2000**, *217*, 271−273.

(25) Hsu, Y.-K.; Lin, Y.-G.; Chen, Y.-C. One-pot Synthesis of $CuFeSe_2$ Cuboid Nanoparticles. *Mater. Res. Bull.* **2011**, *46*, 2117−2119.

(26) Reddy, K. V.; Chetty, S. C. Mössbauer Studies on $CuFeSe_2$. *Mater. Res. Bull.* **1976**, *11*, 55−60.

(27) Delgado, J. M.; De Delgado, G. D.; Quintero, M.; Woolley, J. C. The Crystal Structure of Copper Iron Selenide, $CuFeSe_2$. *Mater. Res. Bull.* **1992**, *27*, 367−373.

(28) Deka, S.; Genovese, A.; Zhang, Y.; Miszta, K.; Bertoni, G.; Krahne, R.; Giannini, C.; Manna, L. Phosphine-Free Synthesis of p-Type Copper(I) Selenide Nanocrystals in Hot Coordinating Solvents. *J. Am. Chem. Soc.* **2010**, *132*, 8912−8914.

(29) Hessel, C. M.; Pattani, V. P.; Rasch, M.; Panthani, M. G.; Koo, B.; Tunnell, J. W.; Korgel, B. A. Copper Selenide Nanocrystals for Photothermal Therapy. *Nano Lett.* **2011**, *11*, 2560−2566.

(30) Li, W.; Zamani, R.; Ibáñez, M.; Cadavid, D.; Shavel, A.; Morante, J. R.; Arbiol, J.; Cabot, A. Metal Ions to Control the Morphology of Semiconductor Nanoparticles: Copper Selenide Nanocubes. *J. Am. Chem. Soc.* **2013**, *135*, 4664−4667.

(31) Lamazares, J.; Jaimes, E.; D'Onofrio, L.; Gonzalez-Jimenez, F.; Porras, G. S.; Tovar, R.; Quintero, M.; Gonzalez, J.; Woolley, J. C.; Lamarche, G. Magnetic Susceptibility, Transport and Mössbauer Measurements in $CuFeSe_2$. *Hyperfine Interact.* **1991**, *67*, 517−521.

(32) Lamazares, J.; Gonzalez-Jimenez, F.; Jaimes, E.; D'Onofrio, L.; Iraldi, R.; Sanchez-Porras, G.; Quintero, M.; Gonzalez, J.; Woolley, J. C.; Lamarche, G. Magnetic, Transport, X-ray Diffraction and Mössbauer Measurements on $CuFeSe_2$. *J. Magn. Magn. Mater.* **1992**, *104*, 997−998.

(33) Ahmadi, M.; Pramana, S. S.; Batabyal, S. K.; Boothroyd, C.; Mhaisalkar, S. G.; Lam, Y. M. Synthesis of Cu_2SnSe_3 Nanocrystals for Solution Processable Photovoltaic Cells. *Inorg. Chem.* **2013**, *52*, 1722−1728.

(34) Wang, J.-J.; Liu, P.; Seaton, C. C.; Ryan, K. M. Complete Colloidal Synthesis of Cu_2SnSe_3 Nanocrystals with Crystal Phase and Shape Control. *J. Am. Chem. Soc.* **2014**, *136*, 7954−7960.

(35) Han, S. K.; Gu, C.; Gong, M.; Wang, Z. M.; Yu, S. H. Colloidal Synthesis of Ternary $AgFeS_2$ Nanocrystals and Their Transformation to Ag_2S-Fe_7S_8 Heterodimers. *Small* **2013**, *9*, 3765−3769.

(36) Langevin, M.-A.; Ritcey, A. M.; Allen, C. N. Air-Stable Near-Infrared $AgInSe_2$ Nanocrystals. *ACS Nano* **2014**, *8*, 3476−3482.

(37) Shao, G.; Chen, G.; Zuo, J.; Gong, M.; Yang, Q. Organometallic Synthesis, Structure Determination, Shape Evolution, and Formation Mechanism of Hexapod-like Ternary $PbSe_xS_{1-x}$ Nanostructures with Tunable Compositions. *Langmuir* **2014**, *30*, 7811−7822.

(38) Shao, G.; Chen, G.; Yang, W.; Ding, T.; Zuo, J.; Yang, Q. Organometallic-Route Synthesis, Controllable Growth, Mechanism Investigation, and Surface Feature of PbSe Nanostructures with Tunable Shapes. *Langmuir* **2014**, *30*, 2863−2872.

(39) Liu, X.; Wang, X.; Zhou, B.; Law, W. C.; Cartwright, A. N.; Swihart, M. T. Size-Controlled Synthesis of $Cu_{2-x}E$ (E = S, Se) Nanocrystals with Strong Tunable Near-Infrared Localized Surface Plasmon Resonance and High Conductivity in Thin Films. *Adv. Funct. Mater.* **2013**, *23*, 1256−1264.

DOI: 10.1021/am508844w
ACS Appl. Mater. Interfaces 2015, 7, 2235−2241

(40) Woolley, J. C.; Lamarche, A.-M.; Lamarche, G.; Brun del Re, R.; Quintero, M.; Gonzalez-Jimenez, F.; Swainson, I. P.; Holden, T. M. Low Temperature Magnetic Behaviour of $CuFeSe_2$ from Neutron Diffraction Data. *J. Magn. Magn. Mater.* **1996**, *164*, 154−162.
(41) Lu, A. H.; Salabas, E. L.; Schüth, F. Magnetic Nanoparticles: Synthesis, Protection, Functionalization, and Application. *Angew. Chem., Int. Ed.* **2007**, *46*, 1222−1244.
(42) Demortière, A.; Panissod, P.; Pichon, B. P.; Pourroy, G.; Guillon, D.; Donnio, B.; Bégin-Colin, S. Size-dependent Properties of Magnetic Iron Oxide Nanocrystals. *Nanoscale* **2011**, *3*, 225−232.
(43) Kodama, R. H.; Berkowitz, A. E.; McNiff, E. J., Jr; Foner, S. Surface Spin Disorder in $NiFe_2O_4$ Nanoparticles. *Phys. Rev. Lett.* **1996**, *77*, 394−397.
(44) Batlle, X.; Labarta, A. Finite-size Effects in Fine Particles: Magnetic and Transport Properties. *J. Phys. D: Appl. Phys.* **2002**, *35*, R15−R42.

DOI: 10.1021/am508844w
ACS Appl. Mater. Interfaces 2015, 7, 2235−2241